

Lamb wave TDTE super-resolution imaging assisted by deep learning

Liu-Jia Sun(孙刘家), Qing-Bang Han(韩庆邦), and Qi-Lin Jin(靳琪琳)

Citation: Chin. Phys. B, 2025, 34 (**1**): 014301. DOI: 10.1088/1674-1056/ad886d
Journal homepage: http://cpb.iphy.ac.cn; http://iopscience.iop.org/cpb

What follows is a list of articles you may be interested in

Microcrack localization using a collinear Lamb wave frequency-mixing technique in a thin plate

Ji-Shuo Wang(王积硕), Cai-Bin Xu(许才彬), You-Xuan Zhao(赵友选), Ning Hu(胡宁), and Ming-Xi Deng(邓明晰)
Chin. Phys. B, 2022, 31 (**1**): 014301. DOI: 10.1088/1674-1056/ac0da8

Location of micro-cracks in plates using time reversed nonlinear Lamb waves

Yaoxin Liu(刘尧鑫), Aijun He(何爱军), Jiehui Liu(刘杰惠), Yiwei Mao(毛一葳), Xiaozhou Liu(刘晓宙)
Chin. Phys. B, 2020, 29 (**5**): 054301. DOI: 10.1088/1674-1056/ab81f7

Micro-crack detection of nonlinear Lamb wave propagation in three-dimensional plates with mixed-frequency excitation

Wei-Guang Zhu(祝伟光), Yi-Feng Li(李义丰), Li-Qiang Guan(关立强), Xi-Li Wan(万夕里), Hui-Yang Yu(余辉洋), Xiao-Zhou Liu(刘晓宙)
Chin. Phys. B, 2020, 29 (**1**): 014302. DOI: 10.1088/1674-1056/ab5931

Lamb waves topological imaging combining with Green's function retrieval theory to detect near filed defects in isotropic plates

Hui Zhang(张辉), Hai-Yan Zhang(张海燕), Meng-Yun Xu(徐梦云), Guo-Peng Fan(范国鹏), Wen-Fa Zhu(朱文发), Xiao-Dong Chai(柴晓冬)
Chin. Phys. B, 2019, 28 (**7**): 074301. DOI: 10.1088/1674-1056/28/7/074301

Generation of narrowband Lamb waves based on the Michelson interference technique

Tian-Ming Ye(叶天明), Yan-Feng Xu(徐琰锋), Wen-Xiang Hu(胡文祥)
Chin. Phys. B, 2018, 27 (**5**): 054301. DOI: 10.1088/1674-1056/27/5/054301

Lamb wave TDTE super-resolution imaging assisted by deep learning

Liu-Jia Sun(孙刘家), Qing-Bang Han(韩庆邦)[†], and Qi-Lin Jin(靳琪琳)

College of Information Science and Engineering, Hohai University, Changzhou 213200, *China*

(Received 12 September 2024; revised manuscript received 8 October 2024; accepted manuscript online 18 October 2024)

Ultrasonic Lamb waves undergo complex mode conversion and diffraction at non-penetrating defects, such as plate corrosion and cracks. Lamb wave imaging has a resolution limit due to the guided wave dispersion characteristics and Rayleigh criterion limitations. In this paper, a full convolutional network is designed to segment and reconstruct the received signals, enabling the automatic identification of target modalities. This approach eliminates clutter and mode conversion interference when calculating direct and accompanying acoustic fields in time-domain topological energy (TDTE) imaging. Subsequently, the measured accompanying acoustic field is reversed for adaptive focusing on defects and enhance the imaging quality. To circumvent the limitations of the Rayleigh criterion, the direct acoustic field and the accompanying acoustic field were fused to characterize the pixel distribution in the imaging region, achieving Lamb wave super-resolution imaging. Experimental results indicate that compared to the sign coherence factor-total focusing method (SCF-TFM), the proposed method achieves a 31.41% improvement in lateral resolution and a 29.53% increase in signal-to-noise ratio for single-blind-hole defects. In the case of multiple-blind-hole defects with spacings greater than the Rayleigh criterion resolution limit, it exhibits a 27.23% enhancement in signal-to-noise ratio. On the contrary, when the defect spacings are relatively smaller than the limit, this method has a higher resolution limit than SCF-TFM in super-resolution imaging.

Keywords: Lamb waves, asymmetric defects, fully convolutional network, time-domain topological energy imaging, super-resolution

PACS: 43.35.+d, 43.25.+y, 43.20.Mv

DOI: 10.1088/1674-1056/ad886d **CSTR:** 32038.14.CPB.ad886d

1. Introduction

Ultrasonic phased arrays achieve the deflection and focusing of the acoustic beam by precisely controlling the excitation timing across array elements. This technology allows for real-time sweeping of objects and finds extensive applications in industrial nondestructive testing.[1–5] However, phased array-based imaging exhibits a law of focusing acoustic beams, typically in a fan-sweeping form with a restricted detection range. The total focusing method (TFM) technique is employed to process array data to increase the resolution imaging range, enabling the refocusing of scattered signals on each pixel point within the detection area.[6–11] Despite these benefits of TFM, the multimodal dispersive Lamb waves tend to introduce artifacts into imaging results. Furthermore, according to the Rayleigh criterion, the diffraction of Lamb waves at defects imposes a limit on the resolution of ultrasonic array imaging systems. Consequently, studies addressing the impact of Lamb wave mode mixing and the constraints of the Rayleigh criterion on imaging outcomes have become focal points in the field of ultrasonic non-destructive testing.

Based on the time-reversal invariance of the wave equation and the reciprocity of the acoustic field, Fink[12,13] proposed the acoustic TR theory. By utilizing multiple piezoelectric transducers to excite and receive ultrasonic signals, an inverted wavefield is generated, and the inverted waves are retransmitted to acquire damage information. This technique mitigates the impacts of Lamb wave dispersion and multimode characteristics on imaging outcomes. In addition, it can expand the computational domain as a means to alleviate the anomalous distribution of imaging pixels caused by mode mixing. Considering the signal phase, Camacho *et al.*[14] proposed phase coherence imaging (PCI) technology in medical research. The PCI applies coherence factors to each sampling point and suppresses clutter influence on scattered waves within the target region based on a statistical analysis of the instantaneous phase of the aperture, greatly enhancing imaging resolution. Additionally, imaging efficiency and quality can be improved following the simplified technical implementation by binarizing the phase of scattered signals, utilizing polarity as a resolving feature, and integrating PCI with the full-matrix focusing method. For instance, Liu[15] introduced an image composite technique for compact rectangular phased piezoelectric transducer arrays, combining TFM and PCI images to partially compensate for the interference of guided wave dispersion characteristics on imaging results. On this basis, Prado *et al.*[16] incorporated amplitude and phase information from received signals and fused TFM and SCF pixels to minimize the blind zones and artifacts in imaging. Compared to imaging principles based on geometric theory, topological imaging deriving from shape optimization emerges as a high-precision ultrasound imaging method. Dominguez *et al.*[17] on the ba-

[†]Corresponding author. E-mail: 20111841@hhu.edu.cn

© 2025 Chinese Physical Society and IOP Publishing Ltd. All rights, including for text and data mining, AI training, and similar technologies, are reserved.

sis of topological asymptotics, transformed the excitation of acoustic waves and the interaction between acoustic waves and defects into the solution of direct and accompanying problems. This innovation largely reduces iterative calculations of topological properties, conferring practical applications. Sun[18] utilized TDTE to achieve Lamb wave TDTE high-resolution imaging of blind-hole defects. Instead, the aforementioned imaging methods only alleviate the interference of multimodal Lamb waves on imaging without addressing this issue.

Deep learning has been successfully applied in object detection and image recognition. Convolutional neural networks are proficient in learning acoustic wave scattering laws from datasets, proving high accuracy in defect identification. Song *et al.*[19] proposed a deep learning model (U-Net) to extract edge features of defects in ultrasonic imaging results, followed by reconstructing the defect morphology to achieve high-resolution ultrasonic imaging. Ewald[20] translated multiple Lamb wave scattering signals into time-frequency maps and established mapping relationships between time-frequency features and defects for comprehensive defect characterization. SU *et al.*[21] localized defects by developing a mapping relationship between the amplitude characteristics of Lamb wave scattering signals and defect locations. The incorporation of deep learning into Lamb wave defect imaging has facilitated high-resolution imaging. The full convolutional network (FCN) presents a promising choice for Lamb wave target modality recognition. Initially designed for image semantic segmentation, FCN differs from conventional convolutional neural networks by providing the probability of each input data point rather than representing the probability of a typical category.[22–26] This unique property makes FCN suitable for Lamb wave target modality selection, enabling the selection of the time window for the target modality based on predicted probabilities. Despite these advantages, a research gap remains on the adoption of FCN for Lamb wave modality identification and its combination with TDTE for multi-defect super-resolution imaging.

This study detected Lamb wave defects with spacings smaller than the resolution limit. An FCN was devised to automatically extract Lamb wave target modalities and eliminate the interference from multimodalities on imaging outcomes. Subsequently, the principles of TDTE imaging algorithms were examined. Additionally, the computations for direct and accompanying acoustic fields were optimized and integrated to enhance the precision of adaptive acoustic focusing. In conclusion, the proposed method was compared with three imaging techniques grounded in geometric principles. The array performance index (API) and signal to noise ratio (SNR) were employed to quantitatively evaluate each method's performance in Lamb wave imaging.

2. Target modality pickup and imaging

The FCN model used for image segmentation differs from Lamb wave mode selection in terms of the required output, which necessitates point-by-point probability and classification. Consequently, the fully connected layer for classification prediction becomes unnecessary, as the recognition of results is achieved through deconvolution of the output mode via upsampling operations. This probability distribution was employed to characterize the likelihood of each point in the time-domain signal becoming a target modality.

2.1. FCN architecture

This paper used the FCN network model (see Fig. 1) to process one-dimensional Lamb wave signals. The experimentally collected Lamb wave normalized curve with 5376 in length was input, and complementary zeros were used in the FCN to ensure an equal-length probability distribution of output. All convolution kernels in this model have a size of 3 and are composed of 14 convolution layers, including the lower and upper sample layers (1:1). Each layer employs a one-dimensional convolution and a rectified linear unit activation function. The down-sampling layer extracted the features from the Lamb wave signals, and the up-sampling converted them to probability distributions. The prediction results were outputted using a sigmoid function.

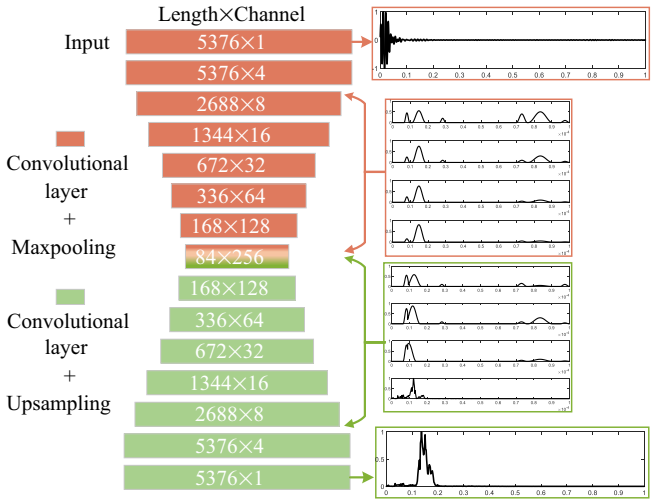


Fig. 1. FCN architecture: length of each layer with channels (left) and extracted channels (right).

Dropout layers with a dropout rate of 0.5 were strategically incorporated into the convolutional layers to mitigate overfitting. Additionally, the number of channels underwent a sequential increase from 1 to 256, followed by a reduction to 1.

2.2. Training

As illustrated in Fig. 2, the dataset for model training is built based on an ultrasonic phased array defect detection experiment. This involved the creation of blind holes at various

locations on an aluminum plate. The experimental setup comprised an M2M ultrasonic phased array detector (M2M company, France), a computer (HP, America), a phased array probe (Shantou ultrasound, China), and an aluminum plate. A total of 9216 sets of ultrasonic Lamb wave signals were generated.

Subsequently, the corresponding scattered wave time window is calculated by the actual distance between the phased bursts and the defects, and the Lamb wave time series sampling points are labeled with two different types: 0 (outside the selected window) and 1 (inside the selected window). The time windows were manually checked to eliminate undesirable results, enhancing the training dataset quality. Ultimately, 8704 high-quality time windows were obtained. Specifically, 6964 units were randomly selected as the training set, with the remaining units constituting the test set. Within the training set, 20% of the samples (9216) were selected as the validation set. This validation set is crucial for adjusting neural network parameters, preventing overfitting, and enhancing the network's generalization capabilities.



Fig. 2. Ultrasonic phased array experimental system and several experimental objects.

By inputting Lamb wave signals and labeled data into the model, the loss function can be defined as follows:

$$H = -\frac{1}{N}\sum_{i=1}^{N}\sum_{t\in T}(q_i^t \log(p_i^t) + (1-q_i^t)\log(1-p_i^t)), \quad (1)$$

where p and q are the predicted and true values of Lamb wave signal phase, respectively. T represents the combination of Lamb wave signal samples in the prediction result, and N represents the total number of trained Lamb wave samples.

The dataset was randomly shuffled and divided into batches, each consisting of 32 samples. The model was trained batch by batch, and its parameters were updated iteratively to minimize the loss function until all batches were processed. Upon confirming the loss curve's stability, training was halted to mitigate the risk of overfitting. The Adam random optimization algorithm was used to optimize the loss function, and the learning rate of 10^{-4} was incorporated into the Keras framework. Using CPU calculation (i5-12500H), the convergence curves of training loss and verification loss as shown in Fig. 3 achieve good convergence in 1000 periods.

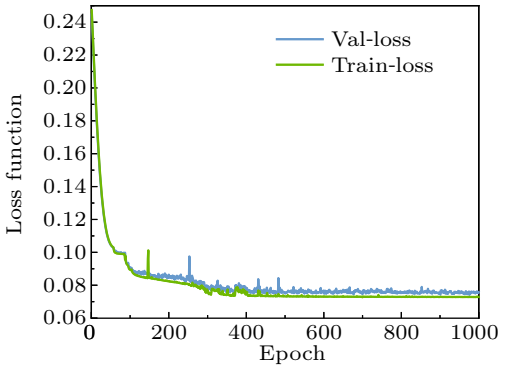


Fig. 3. Relationship between the training loss and verification loss with the number of periods.

2.3. Prediction

As shown in Fig. 4, the FCN model-derived output represents the probability of each sample point in the Lamb wave signal representing the target modality. To transform this probability into a time window, a threshold value was defined to facilitate signal segmentation. Following experiments and human judgment, the threshold was set at 0.15, and time windows smaller than one-half cycle were discarded.

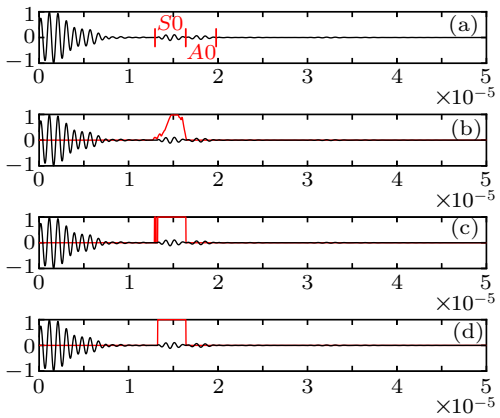


Fig. 4. Windowing results: (a) original Lamb wave signal, (b) the target mode probability distribution, (c) the window after threshold selection, (d) the mode selection results after eliminating the interference window for less than half the period.

2.4. Quantitative performance evaluation of FCN

The performance of the FCN model was characterized by metrics such as accuracy (A), precision (P), recall (R), F1 score, and intersection-over-union (IoU). The true positives (TP) and true negatives (TN) indicate that the frequencies of the FCN model correctly classified a target or non-target modality in the signal samples. The false positives (FP) and false negatives (FN) represent the samples identified as the target modality classified as a non-signal or a non-target modality. The calculation method is written as follows:

$$A = \frac{\mathrm{TP}+\mathrm{TN}}{\mathrm{TP}+\mathrm{FP}+\mathrm{TN}+\mathrm{FN}},$$
$$P = \frac{\mathrm{TP}}{\mathrm{TP}+\mathrm{FP}},$$
$$R = \frac{\mathrm{TP}}{\mathrm{TP}+\mathrm{FN}},$$

$$F1 = 2\frac{P \times R}{P + R}, \tag{2}$$

where TP + FP represents the total number of samples for modal selection of Lamb wave signals by FCN, and TP + FN denotes the sample count of Lamb wave signals in the test set.

IoU was employed to assess the alignment of modal selection results with the target modal time window, defined as follows:

$$\text{IoU} = \frac{\text{Length of overlap}}{\text{Length of union}}. \tag{3}$$

The numerator and denominator in the formula denote the overlap length and concatenation length between the Lamb wave target modes and the model predictions, respectively.

The FCN prediction time window was applied to the test dataset, and the TP, TN, FP, and FN counts were tallied to calculate each evaluation metric. A measures the percentage of correctly identified target modality from Lamb wave samples by the FCN. The average accuracy for the test set is 0.93, indicating that over 93% of the target modalities in the total Lamb wave samples are accurately classified. P is indicative of the reliability of the modality recognition method, representing the ratio of correctly detected target modality to the total Lamb wave signal samples. Impressively, over 95% of the Lamb wave samples are correctly identified.

The R quantifies the percentage of FCN correctly classified target modality in the total Lamb wave samples, yielding an average value of 75% for the test set. The $F1$ score provides a balanced evaluation of P and R performance, reaching 0.87 for FCN. The IoU measures the agreement between the selected time window and the genuine target modality, yielding 0.88 on average for the test set. These metrics collectively signify that the FCN model demonstrates commendable accuracy.

2.5. Optimization of the TDTE imaging method

The challenges associated with the direct and accompanying problems in TDTE imaging necessitate manual selection of scattered waves and consideration of Lamb wave mode conversion during calculations. To streamline the TDTE calculation, an FCN was employed to segment and reconstruct the received signal.

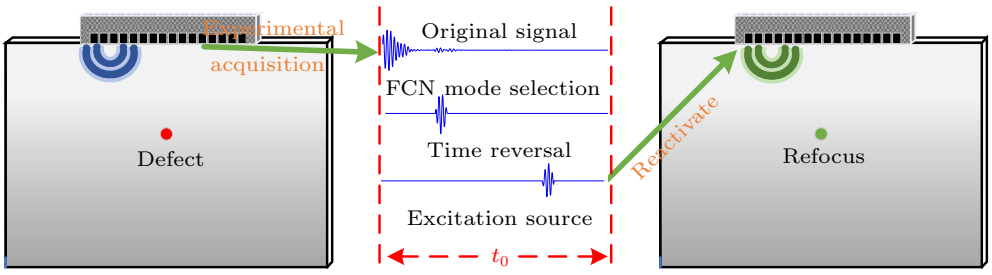


Fig. 5. Schematic diagram of the scattered signal time reversal.

As illustrated in Fig. 5, the excitation pulse signal from the array initiates the direct acoustic field. According to Huygens principle, the interaction between the acoustic wave and the defect leads to signal scattering and reflection. Then, the defect becomes a secondary acoustic source, generating the reversed scattered wave at the defect. This wave re-excites the defect, giving rise to the accompanying acoustic field. The direct and accompanying acoustic fields are multiplied and integrated to derive TDTE values, which were utilized as pixel values for imaging. The specific processes unfold as follows:

(i) Direct acoustic field calculations: The Lamb wave signal was initiated through excitation in the aluminum plate and was extracted as the excitation signal $u_0(t)$. The direct acoustic field is calculated based on Eq. (4) in accordance with the Lamb wave propagation model

$$U(x,y,t) = \mathrm{F}^{-1}\{\mathrm{F}\{u_0(t)\}\,\mathrm{e}^{-\mathrm{i}2\pi f d/c_p^{s0}(f)}\}, \tag{4}$$

where $\mathrm{F}\{\cdot\}$ and $\mathrm{F}^{-1}\{\cdot\}$ represent the Fourier transform and inverse transform, respectively. d denotes the distance between the current pixel point and the defect. $c_p^{s0}(f)$ signifies the phase velocity of the Lamb wave target mode ($S0$) under the corresponding frequency thickness, which is calculated by Rayleigh Lamb equation. The dispersion curves in the aluminum plate are shown in Fig. 6.

(ii) Accompanying acoustic field calculations: The target modality signal extracted from the FCN model was employed, inverted, and re-excited at the corresponding array element. The received signal was used to compute the accompanying acoustic field. In contrast to conventional TDTE imaging, the precise segmentation of the target modality using the FCN model eliminates the need to consider mode conversion in the calculation of the accompanying acoustic field. Consequently, the process can be streamlined as follows:

$$V(x,y,t) = \mathrm{F}^{-1}\left\{\varphi \mathrm{F}\{zj(t)\}\exp\left[\frac{-\mathrm{i}2\pi f d}{c_p^{s0}(f)}\right]\right\}, \tag{5}$$

where φ represents the propagation coefficient of the target modality.

(iii) Fusion of the direct and accompanying acoustic fields: The imaging pixel values are determined using the

TDTE energy calculation Eq. (6)

$$I(x,y) = \int_0^T \|U(x,y,t)\|^2 \|V(x,y,T-t)\|^2 \, \mathrm{d}t, \tag{6}$$

where $\|V(x,y,T-t)\|$ represents the accompanying acoustic field after time reversal, and (x, y) denotes the pixel point position within the imaging region.

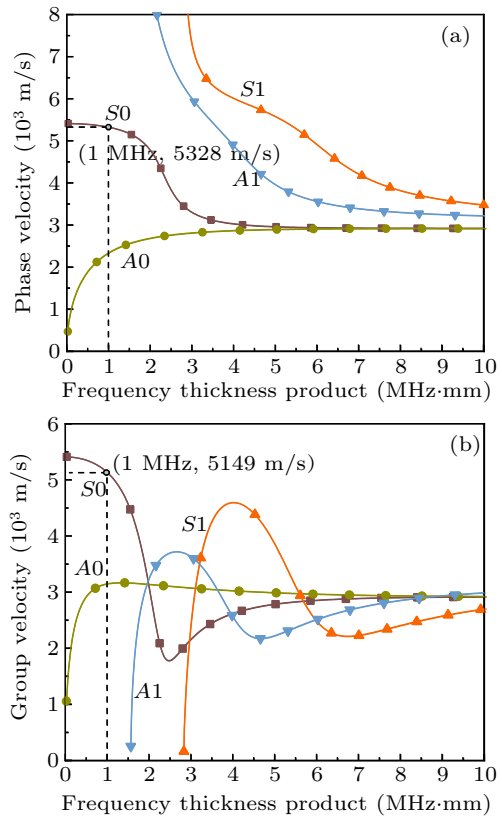


Fig. 6. Aluminum plate dispersion curves: (a) phase velocity, (b) group velocity.

3. Experimental research

3.1. Lamb wave experiment

As shown in Fig. 7, the experimental system consists of a signal generator (Tektronix AFD3152C, US), a signal amplifier, an oscilloscope (Tektronix DPO3024, US), piezoelectric chip (500 kHz, China), and an aluminum plate.

The characteristics of aluminum plate specimens are detailed in Table 1.

Table 1. Parameters of the test plate.

Dimension (mm)	Density (kg/m^3)	Poisson's ratio	Young's modulus (GPa)
$300 \times 300 \times 2$	2.69	0.35	69

The parameters of the piezoelectric chip and the arrangement of the array are shown in Table 2. The experiment employed a five-cycle sine wave signal with a central frequency of 500 kHz (see Fig. 8). Referring to the Lamb wave dispersion curve of the aluminum plate shown in Fig. 6, when the frequency-thickness product is 1 MHz·mm, a relatively pure $S0$ mode signal can be obtained through symmetric excitation.

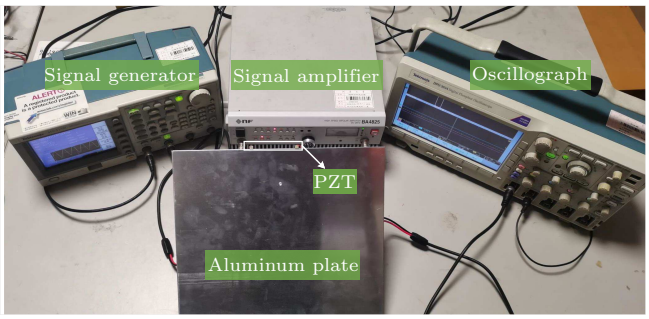


Fig. 7. Ultrasonic array experimental system.

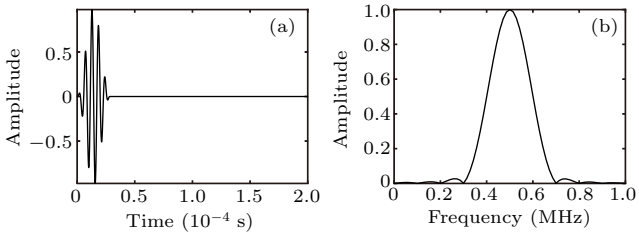


Fig. 8. Excitation signal: (a) time domain diagram, (b) spectrum diagram.

Table 2. Setting of experimental parameters.

Parameter	Property (value)
Array element number	16
Array element length	5 mm
Array element width	5 mm
Array element spacing	1 mm

3.2. Experimental signal analysis

Acoustic diffraction adheres to the Rayleigh criterion. Specifically, the ultrasonic array imaging system cannot effectively differentiate between two target defects when the spacing between neighboring defects falls below a threshold value. This threshold is calculated as follows:

$$d_{\mathrm{R}} = 0.61 \frac{\lambda}{\sin \theta_{\mathrm{R}}}, \tag{7}$$

where λ represents the acoustic wave wavelength in the aluminum plate, and θ_{R} denotes the longitudinal deflection angle from the first array element to the defect center.

As shown in Fig. 9, based on the array size and placement position, x and h are 47.5 mm and 50 mm, respectively. From this figure, we can obtain $\sin \theta_{\mathrm{R}} = 0.689$ and $d_{\mathrm{R}} = 9.4$ mm.

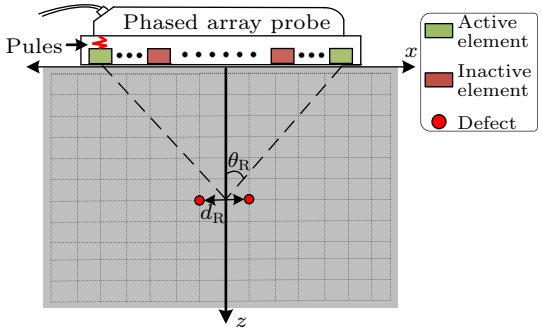


Fig. 9. Schematic diagram of the ultrasound array resolution.

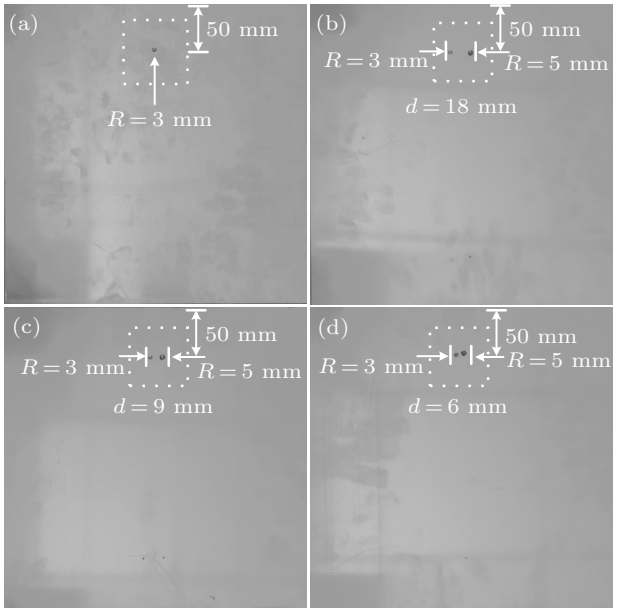


Fig. 10. Aluminum plate specimen.

Figure 10 shows four sets of aluminum plate Lamb wave experiments for validation based on the calculation results of the Rayleigh criterion. The defect depth of the blind hole is half of the thickness of the aluminum plate, and the distance from the upper surface of the aluminum plate is 50 mm. In Fig. 10(a), a single circular blind-hole with a diameter of 3 mm is detectable. Figures 10(b)–10(d) all feature double-blind holes with a 3-mm diameter on the left and a 5-mm diameter on the right, demonstrating defects with spacings of 18 mm (exceed the resolution threshold), 9 mm (slightly less than the resolution threshold), and 6 mm (below the resolution threshold).

In Fig. 11, time-domain Lamb wave signals were acquired from the 8th and 16th array elements in a single-blind-hole defect in the aluminum plate (Z_m^n, where m and n denote the m-th array element excitation and the n-th array element reception, respectively). The scattered signals undergo a mode shift at the blind-hole defects, indicating the presence of two Lamb wave modes, namely, $S0$ and $A0$.

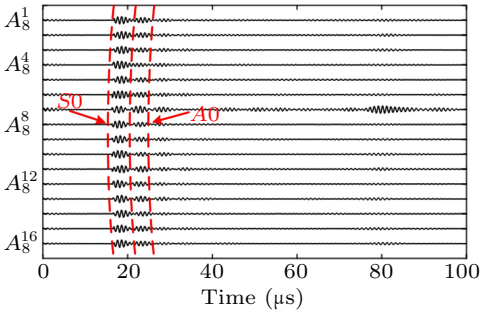


Fig. 11. Time-domain scattering signals of defects in single-blind holes.

3.3. Analysis of imaging results

3.3.1. Analysis of single-blind-hole imaging results

The Lamb wave signals from the single-blind-hole specimen were imaged using TFM, TR, sign coherence factor-total focus method (SCF-TFM), and TDTE. The imaging outcomes are depicted in Fig. 12.

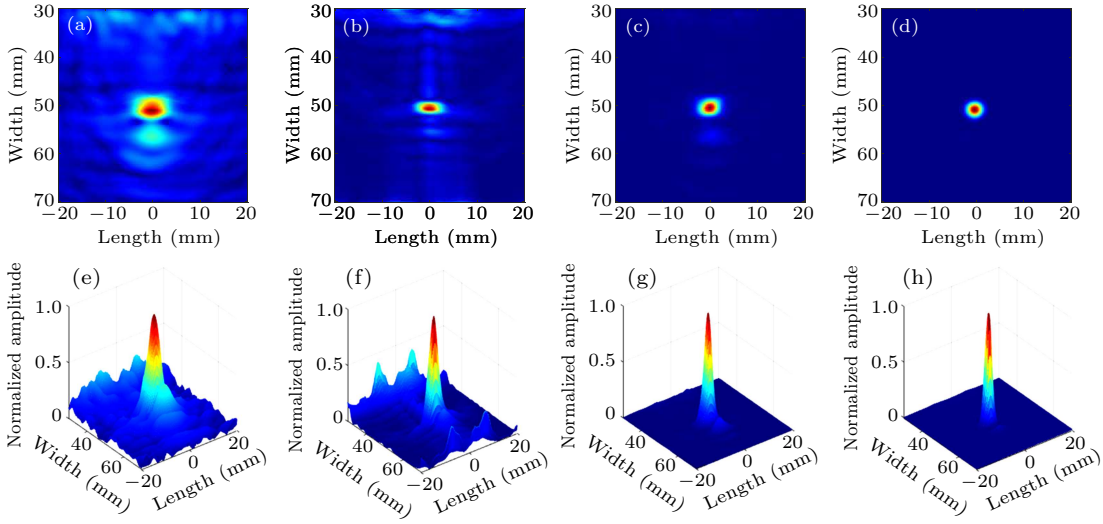


Fig. 12. Single-blind-hole results: (a) TFM, (b) TR, (c) SCF-TFM, (d) TDTE, (e) TFM three-dimensional (3D) image, (f) TR 3D image, (g) SCF-TFM 3D image image, (h) TDTE 3D image.

In the above imaging results, influenced by the multi-modality attribute of Lamb waves, substantial artifacts appeared in the TFM imaging. TR and SCF-TFM suppress the interference of the dispersion effect by enlarging the computation domain and weakening the scattered waves in the non-target region respectively. The TDTE erased mode transformations and noise interference after modality selection based on the FCN model, merging the direct and incidental acoustic fields and achieving the best performance among the four methods.

API and SNR are incorporated for a quantitative assessment of the imaging quality across the four methods. API is

a dimensionless image resolution representation method for point spread function space size

$$\mathrm{API} = A_{-6\ \mathrm{dB}}/\lambda^2, \tag{8}$$

where A is the cross-sectional area of the 3D image corresponding to the intensity threshold of -6 dB in the longitudinal profile, λ is the wavelength corresponding to the center frequency of the Lamb wave.

SNR is the ratio of defect signal to background noise intensity, reflecting the overall quality level of ultrasound imaging, expressed as

$$\mathrm{SNR} = 20\log_{10}\left(\frac{P_{\mathrm{signal}}}{P_{\mathrm{noise}}}\right), \tag{9}$$

where P_{signal} and P_{noise} represent the peak value of the defect signal and the mean value of the background noise, respectively.

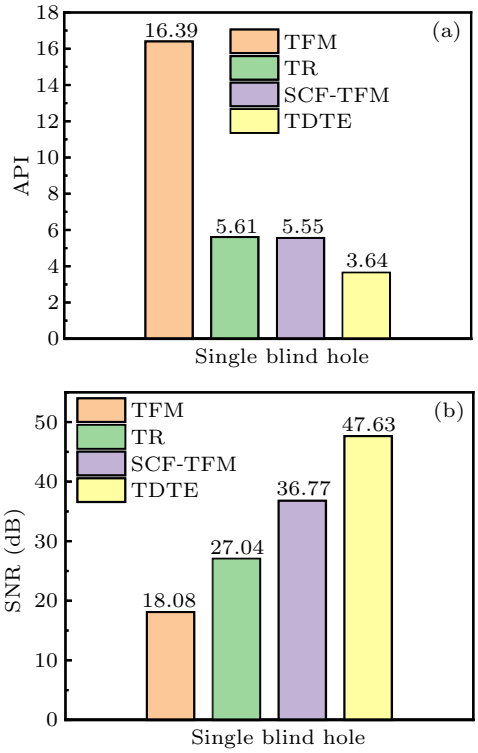


Fig. 13. Performance metrics of different imaging algorithms for single-blind-hole defects: (a) API, (b) SNR.

In the single-blind-hole imaging results for aluminum plates, the descending sequence of API is $\mathrm{API_{TFM}} > \mathrm{API_{TR}} > \mathrm{API_{SCF-TFM}} > \mathrm{API_{TDTE}}$, and the ascending order for SNR is $\mathrm{SNR_{TFM}} < \mathrm{SNR_{TR}} < \mathrm{API_{SCF-TFM}} < \mathrm{SNR_{TDTE}}$. The figure above illustrates that TDTE exhibits improvements of 77.79%, 35.12%, and 34.41% in API compared to TFM, TR, and SCF-TFM, respectively. Regarding SNR, it increases by 163.44%, 76.15%, and 29.53%, respectively.

Figure 14 compares the lateral intensity curves for the four imaging methods. With a limit of -6 dB, the TDTE main lobe displays a smaller peak width than SCF-TFM (approximately 1.31 mm versus 1.91 mm) and a 31.41% higher lateral resolution than SCF-TFM.

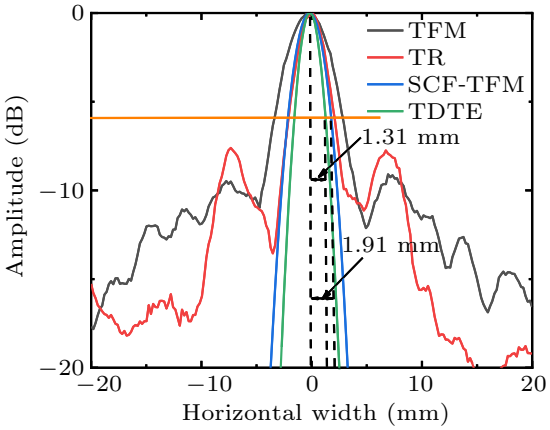


Fig. 14. Comparison of transverse amplitude curves.

Overall, the imaging quality index of a single blind hole Lamb wave indicates that the imaging performance of TDTE optimized by FCN model modal selection is far superior to the other three methods, and can better characterize defect location and morphology information.

3.3.2. Comparative analysis of imaging results for asymmetric blind-hole defects featuring spacings greater than resolution threshold

According to Fig. 15, when detecting an asymmetric blind-hole defect with a spacing of 18 mm (greater than the resolution threshold), all imaging methods can effectively identify the two defects.

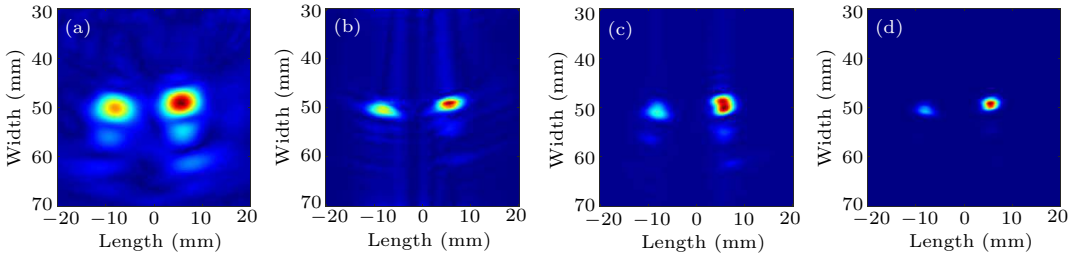


Fig. 15. Results of asymmetric 18-mm spacing defects: (a) TFM, (b) TR, (c) SCF-TFM, (d) TDTE.

The corresponding quantitative evaluation indexes are presented in Fig. 16. Compared to TFM, TR, and SCF-TFM, the TDTE exhibits improvements of 85.29%, 46.59%, and 45.39% in API, respectively. Regarding SNR, this algorithm demonstrates

enhancements of 116.20%, 54.75%, and 27.23% compared to the other three methods.

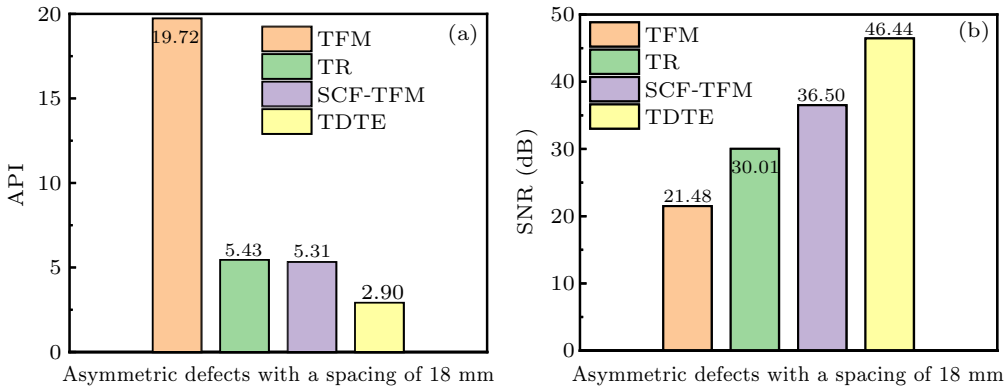


Fig. 16. Performance indicators of different imaging algorithms for asymmetric 18-mm spacing defects: (a) API, (b) SNR.

3.3.3. Comparative analysis of imaging results for asymmetric blind-hole defects with spacings slightly smaller than resolution threshold

As shown in Fig. 17, for asymmetric blind-hole defects with a 9-mm spacing slightly smaller than the resolution threshold, TFM fails to distinguish between these defects effectively. TR and SCF-TFM show multiple artifacts and only TDTE displays a good recognition capacity.

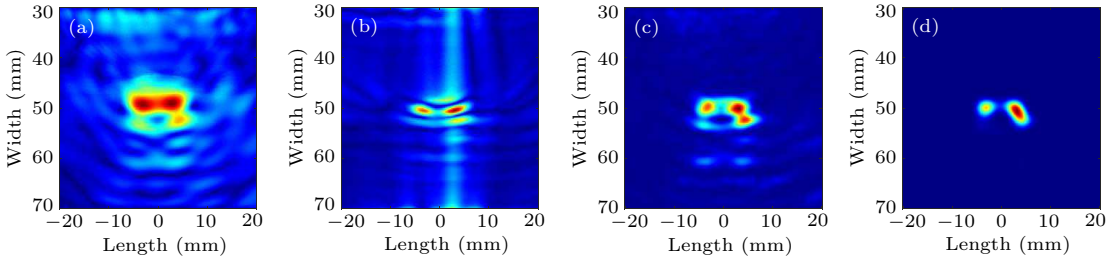


Fig. 17. Results of asymmetric 9-mm spacing defects: (a) TFM, (b) TR, (c) SCF-TFM, (d) TDTE.

The imaging quantitative evaluation indexes of the four modalities are shown in Fig. 18, with $\mathrm{API_{TR}} > \mathrm{API_{SCF-TFM}} > \mathrm{API_{TDTE}}$, and $\mathrm{SNR_{TR}} < \mathrm{API_{SCF-TFM}} < \mathrm{SNR_{TDTE}}$. In terms of API, TDTE exhibits 34.05% and 29.52% improvements compared to TR and SCF-TFM, respectively; in addition, its relative enhancements in SNR are 57.10% and 15.49%, respectively.

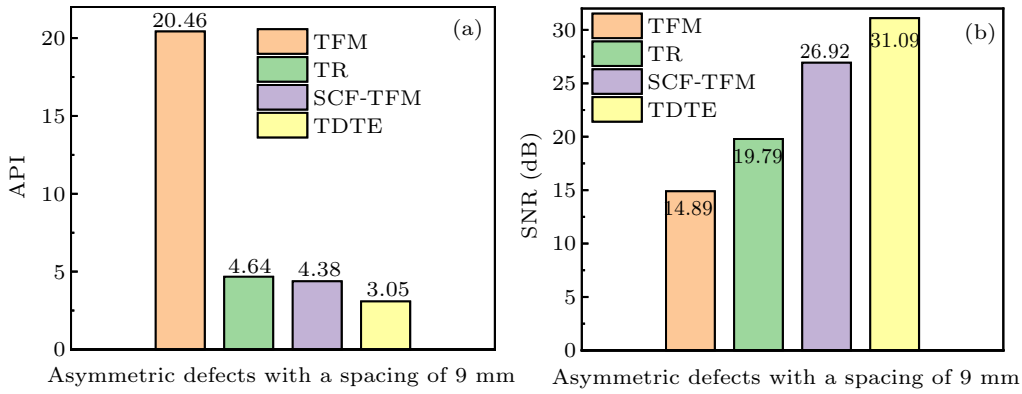


Fig. 18. Performance indicators of different imaging algorithms for asymmetric 9-mm spacing defects: (a) API, (b) SNR.

3.3.4. Assessment of imaging results for asymmetric blind-hole defects (with spacings below resolution threshold)

As shown in Fig. 19, in the presence of asymmetric blind-hole defects with a spacing of 6 mm (smaller than the resolution threshold), TFM, TR, and SCF-TFM cannot effectively distinguish between the two defects. In contrast, TDTE maintains its ability to discern asymmetry despite slight artifacts observed in the imaging results.

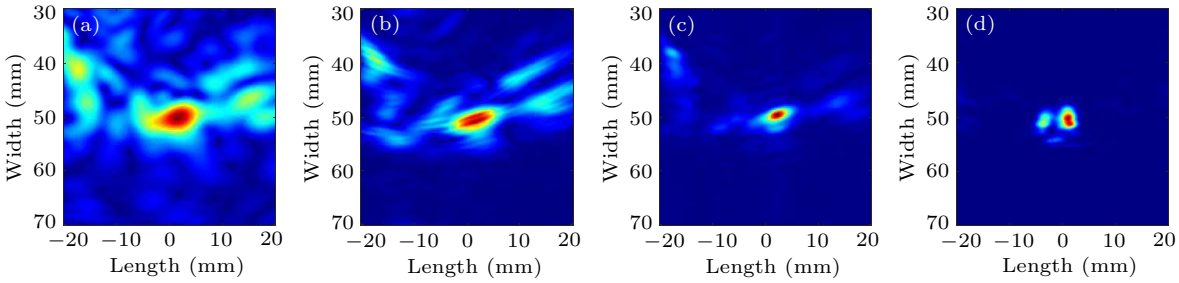


Fig. 19. Results of asymmetric 6-mm spacing defects: (a) TFM, (b) TR, (c) SCF-TFM, (d) TDTE.

As depicted in Fig. 20, the TDTE-based calculation of the transverse amplitude profile at the 50-mm depth of the blind hole demonstrates that two distinct peaks persist on the transverse intensity profile at a threshold of −6 dB with $\tau = -12.83$. This observation indicates that TDTE imaging, under the guidance of FCN model-identified modality, can recognize asymmetric blind-hole defects with a spacing smaller than the resolution threshold.

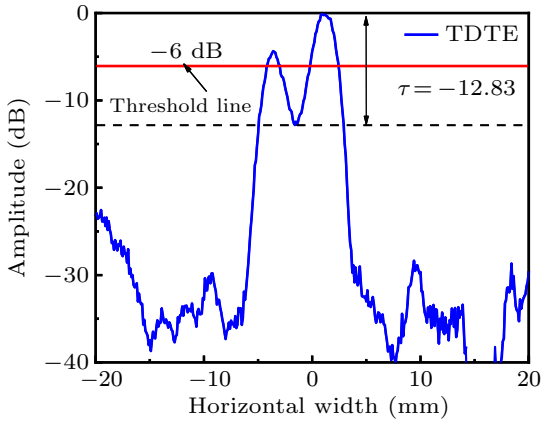


Fig. 20. Transverse amplitude curve of TDTE imaging for asymmetric defects of 6-mm spacing.

4. Conclusion

In this study, an FCN network for target mode selection was introduced to enhance the resolution of Lamb wave imaging. Additionally, the Lamb wave TDTE imaging method was optimized based on the mode selection results. Subsequently, ultrasonic Lamb wave detection experiments were conducted on aluminum plates.

In the case of a single-blind-hole defect, the four methods consistently and accurately depict its location and morphology. Furthermore, TR, SCF-TFM, and TDTE effectively mitigate the Lamb wave scattering effects. Notably, TDTE demonstrates the highest lateral resolution among these methods. When the defect spacing is greater than the resolution threshold, the TFM imaging performance index is the worst. Specifically, TDTE exhibits the most favorable imaging outcomes, with a remarkable improvement of 77.79% in API and a significant 163.44% enhancement in SNR compared to TFM. In the case of asymmetric blind holes having defect spacings slightly below the resolution threshold, TFM cannot effectively discern the defects. TR and SCF-TFM show artifacts. TDTE stands out with superior imaging quality and demonstrates notable improvements compared to TR and SCF-TFM, enhancing API by 34.05% and 29.52% and elevating SNR by 57.10% and 15.49%, respectively. When the spacing is further smaller than the Rayleigh criterion, the three traditional methods are no longer able to accurately reflect the defect morphology. Despite such a limitation, TDTE still proves capable of super-resolution imaging.

In conclusion, the use of FCN networks to eliminate the interference of Lamb wave mode conversion and noise to improve defect recognition can assist TDTE to achieve super-resolution imaging.

Acknowledgements

Project supported by the National Natural Science Foundation of China (Grant No. 12174085), the Key Research and Development Project of Changzhou, Jiangsu Province, China (Grant No. CE20235054), and the Postgraduate Research and Practice Innovation Program of Jiangsu Province, China (Grant No. KYCX24_0833).

References

[1] Ding X Y, Zhao Y X, Deng M X, Shui G S and Hu N 2020 *Int. J. Mech. Sci.* **171** 105371
[2] Sun M X and Qu J M 2020 *Ultrasonics* **108** 106180
[3] Wang J S, Xu C B, Zhao Y X, Hu N and Deng M X 2020 *Materials* **13** 3318
[4] Huan Q, Chen M T, Su Z Q and Li F X 2019 *Ultrasonics* **97** 29
[5] Nicolas Quaegebeur and Patrice Masson 2012 *Ultrasonics* **52** 1056
[6] Dai Y X, Yan S G and Zhang B X 2021 *Chin. Phys. B* **30** 074301
[7] Li F Z and Luo Y 2021 *Acta Mechanica Solida Sinica* **34** 404
[8] Cheng T, *et al.* 2024 *Chin. Phys. B* **33** 040303
[9] Zhu W F, Xiang Y X and Zhang H Y, *et al.* 2023 *Mech. Syst. Signal Pr.* **190** 110121
[10] Wang J S, *et al.* 2022 *Chin. Phys. B* **31** 014301
[11] Zhang W J, Chai X D, Zhu W F, Zheng S B, Fan G P, Li Z W, Zhang H and Zhang H F 2023 *Meas. Sci. Technol.* **34** 055406
[12] Fink M 1992 *IEEE Trans. Ultrason. Ferroelect. Freq. Contr.* **39** 555

[13] Fink M 2001 *J. Acoust. Soc. Am.* **110** 2615
[14] Camacho J, Brizuela J and Fritsch C 2010 *American Institute of Physics* **1211** 855
[15] Liu Z H, Sun K M, Song G R, He C F and Wu B 2016 *Mech. Syst. Signal Pr.* **70–71** 625
[16] Prado V, Higuti R, Kitano C, *et al.* 2013 *NDT & E International* **59** 86
[17] Dominguez N and Gibiat V 2010 *Ultrasonics* **50** 367
[18] Sun L J, Zhu W F, Shao W, *et al.* 2021 *Sensors and Actuators A: Physical* **332** 113102
[19] Song H M and Yang Y C 2020 *NDT & E International* **116** 102344
[20] Ewald V, Sridaran R, Venkat A, *et al.* 2021 *Mech. Syst. Signal Pr.* **165** 108153
[21] Su C H, Jiang M S and Lv S S, *et al.* 2019 *IEEE Sensors Journal* **19** 5784
[22] Hu L L, Zheng X D, Duan Y T, Yan X F, Hu Y and Zhang X L 2018 *Geophysics* **84** U45
[23] Mousavi S M, Ellsworth W L, Zhu W Q, *et al*. 2020 *Nat. Commun.* **11** 3952
[24] Jiang W B, Xi C P and Wang W C, *et al*. 2021 *IEEE Transactions on Geoscience and Remote Sensing* **60** 5903610
[25] Yuan S Y, Liu J W and Wang S X, *et al*. 2017 *IEEE Geoscience and Remote Sensing Letters* **15** 272
[26] Zhu W Q and Beroza G C 2019 *Geophysical Journal International* **216** 261